

# CROSSFLOW AND GÖRTLER INSTABILITIES IN HYPERSONIC BOUNDARY LAYERS

Youcheng, Xi1 & Song, Fu1

<sup>1</sup>School of Aerospace engineering, Tsinghua University, Beijing China, 100084

#### **Abstract**

In three-dimensional hypersonic boundary layers, the crossflow and Görtler instabilities are of great importance and may trigger transition. Using the numerical simulations, stability theory, and together with some ideas from classical differential geometry, we found the origin of both crossflow and Görtler instabilities over a three-dimensional hypersonic boundary layer are because of the bending of local inviscid streamline. The appearance of which instabilities depends on the ratio between the normal curvature and geodesic curvature. The study suggests that as the crossflow increase, the geodesic curvature of the inviscid streamline would become much larger than the normal curvature, which shows that the crossflow instability is the dominative at larger swept angles. The influences of crossflow and surface curvature on the nonlinear developments are also discussed.

Keywords: Crossflow instability, Görtler instability, Hypersonic, three-dimensional boundary layer

#### 1. Introduction

Laminar-turbulence transition of boundary layer flows has obvious influence on the performance of hypersonic vehicles because of the great differences for surface skin friction and aerodynamic heating under laminar or turbulent conditions. During the designing, special attentions have been put on the fundamental instability mechanisms that cause transition of boundary layer at the inlet of scramjet. The inlets of scramjet are usually made up by the combination of several three-dimensional curved surfaces, from the leading edge to the scramjet, which makes it difficult to understand the transition mechanism directly. Therefore, a simplified three-dimensional boundary layer flow over a concave wall, which the fundamental characteristics are kept, is used to understand the mechanism. Under this configuration, two kinds of stationary instability may occur. One is the cross-flow instability caused by the imbalance between pressure gradient and centripetal acceleration, which appears as co-rotating vortices whose axes are aligned to the local inviscid streamlines, within a few degrees. The other is the Görtler instability induced by the imbalance between inertial and centrifugal forces, which forms the streamwise-oriented, counter-rotating vortices.

In this paper, we want to clarify two questions. The first is to identify which mechanisms are the dominate in hypersonic boundary layer if both crossflow and the concave surface appear. The second is to understand the relationship or transformation between these two stationary instabilities.

# 2. Model and Methodology

## 2.1 Model and governing equation

The swept model, with a sweep angle  $\Lambda$ , consists of a cylindrical head with radius  $R_1$ , followed by a 105 mm-long flared body, generated by a circular curve with a radius  $R_2$  and a plate at the end. The whole computational domain is bounded by the shock and wall surface as sketched in figure 1. The unit freestream Reynolds number  $Re_s$ , the sweep Reynolds number  $Re_s$ , the freestream Mach

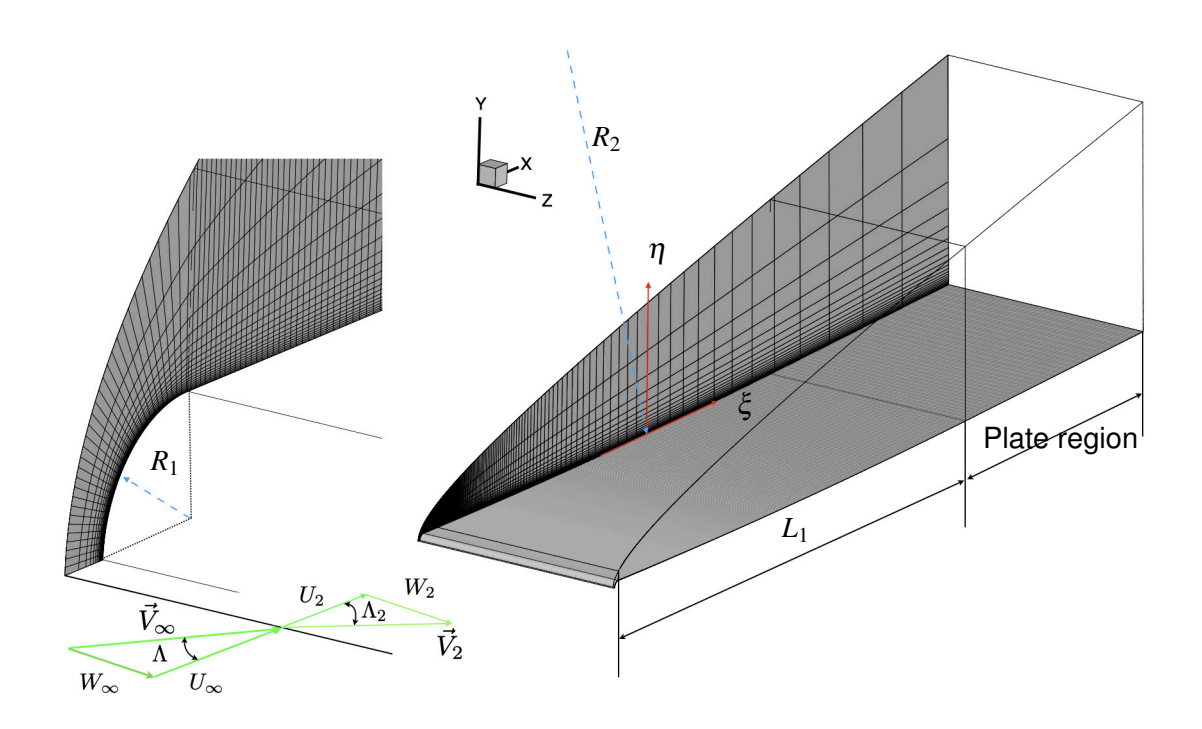


Figure 1 – Sketch of the model and the coordinates. The whole computational domain is bounded by the shock surface and wall surfaces. A plate region is added at the end of the computational domain. The mesh on the x-y plane, has been plotted every 7 points in the  $\eta$  direction (surface normal direction) and every 20 points in the  $\xi$  direction (surface tangent direction).

	$M_{\infty}$	$M_{s}$	$M_{\infty}^n$	Λ	Pr	γ	$Re_{\infty}$	$Re_s$	$T_{\infty}$	$T_w$
Case 1	8.5	0.00	8.50	$0^o$	0.72	1.4	$1.4586 \times 10^{7}$	0.0	50.64K	658.32K
Case 2	8.5	0.19	8.47	$5^o$	0.72	1.4	$1.4586 \times 10^{7}$	13.12	50.64K	658.32K
Case 3	8.5	0.39	8.37	$10^{o}$	0.72	1.4	$1.4586 \times 10^{7}$	26.29	50.64K	658.32K
Case 4	8.5	0.59	8.21	$15^{o}$	0.72	1.4	$1.4586 \times 10^{7}$	39.54	50.64K	658.32K
Case 5	8.5	0.80	7.99	$20^{o}$	0.72	1.4	$1.4586 \times 10^{7}$	52.89	50.64K	658.32K
Case 6	8.5	1.02	7.70	$25^{o}$	0.72	1.4	$1.4586 \times 10^{7}$	66.38	50.64K	658.32K
Case 7	8.5	1.25	7.36	$30^{o}$	0.72	1.4	$1.4586 \times 10^{7}$	80.03	50.64K	658.32K
Case 8	8.5	1.51	6.96	$35^{o}$	0.72	1.4	$1.4586 \times 10^{7}$	93.84	50.64K	658.32K
Case 9	8.5	1.8	6.51	$40^{o}$	0.72	1.4	$1.4586 \times 10^{7}$	107.76	50.64K	658.32K
				F	$R_1$	$R_2$	$L_1$			
1mm 2000mm 105mm										

Table 1 – Simulation conditions and geometrical parameters.

number  $M_{\infty}$ , the sweep Mach number  $M_s$ , the normal Mach number  $M_{\infty}^n$  and the recovery temperature  $T_r$  are defined as

$$Re_{\infty} = \frac{|\vec{V}_{\infty}|}{v_{\infty}}, Re_{s} = \frac{W_{\infty}\delta^{*}}{v_{r}}, M_{\infty} = \frac{|\vec{V}_{\infty}|}{c_{\infty}}, M_{s} = \frac{W_{\infty}}{c_{s}}, M_{\infty}^{n} = \frac{U_{\infty}}{c_{\infty}} = M_{\infty}\cos\Lambda$$

$$T_{r} = T_{\infty} + \zeta(T_{0} - T_{\infty}), \text{where } \zeta = 1 - (1 - \xi_{w})\sin^{2}\Lambda.$$
(1)

Here,  $\xi_w$  is a constant for specific freestream conditions ( $M_\infty$  and  $\Lambda$ ) and determined based on the study of [1];  $R_1$  represents the radius of the leading-edge;  $\vec{V}_\infty$  stands for the freestream velocity vectors with  $U_\infty, V_\infty$  and  $W_\infty$  along x, y and z direction, respectively.  $T_\infty$  and  $T_0$  stand for the freestream and stagnation temperature, respectively. The parameters  $c_\infty$  and  $c_s$  are the sound speed before and after the leading shock,  $v_r$  represents the kinematic viscosity at  $T_r$ .  $\delta^*$  is defined as  $\delta^* = \sqrt{v_r R_1/2U_2}$ , where  $U_2$  represents chord-wise velocity behind the shock. The Prandtl number  $P_r$  and the specific heat ratio  $\gamma$  are set following the ideal gas assumption of air. The physical and geometrical parameters are listed in table 1.

The motion of compressible flows is governed by Navier-Stokes equations. The set of non-dimensional equations in Cartesian coordinates  $x_1 = x, x_2 = y, x_3 = z$  can be written as

$$\frac{\partial \mathbf{Q}}{\partial t} + \frac{\partial \mathbf{F}_{j}}{\partial x_{i}} + \frac{\partial \mathbf{F}_{vj}}{\partial x_{i}} = 0, \tag{2a}$$

$$\mathbf{Q} = \begin{bmatrix} \rho \\ \rho u_1 \\ \rho u_2 \\ \rho u_3 \\ E_t \end{bmatrix}, \mathbf{F}_j = \begin{bmatrix} \rho u_j \\ \rho u_1 u_j + p \delta_{1j} \\ \rho u_2 u_j + p \delta_{2j} \\ \rho u_3 u_j + p \delta_{3j} \\ (E_t + p) u_j \end{bmatrix}, \mathbf{F}_{vj} = \begin{bmatrix} 0 \\ \tau_{1j} \\ \tau_{2j} \\ \tau_{3j} \\ \tau_{jk} u_k - q_j \end{bmatrix},$$
(2b)

where  $u_1 = u, u_2 = v$  and  $u_3 = w$  stands for the velocity along the coordinates x, y, z, respectively. t stands for the time. The total energy  $E_t$  and the viscous stress  $\tau_{ij}$  are given as, respectively,

$$E_{t} = \rho \left( \frac{T}{\gamma(\gamma - 1)M^{2}} + \frac{u_{k}u_{k}}{2} \right), \quad \tau_{ij} = \frac{\mu}{Re_{\infty}} \left( \frac{\partial u_{i}}{\partial x_{j}} + \frac{\partial u_{j}}{\partial x_{i}} - \frac{2}{3} \delta_{ij} \frac{\partial u_{k}}{\partial x_{k}} \right). \tag{3}$$

The pressure p and heat flux  $q_i$  are obtained from:

$$p = \frac{\rho T}{\gamma M_{\infty}^2}, \quad q_i = -\frac{\mu}{(\gamma - 1)M_{\infty}^2 RePr} \frac{\partial T}{\partial x_i}.$$
 (4)

The viscosity is calculated using the Sutherland law

$$\mu = T^{3/2} \frac{T_{\infty} + C^*}{TT_{\infty} + C^*},\tag{5}$$

with  $C^* = 110.4K$ .

#### 2.2 Code features

The first code we use to perform computations of unperturbed boundary layer is the high-order finite difference code developed recently at Tsinghua University [2, 3, 4]. A shock-fitting method [5] is used to compute steady hypersonic viscous flow together with the high-order accurate non-compact central finite differences methods. The fifth-order upwind scheme (for inviscid flux  $F_j$ ) and the 6th-order centre scheme (for viscous flux  $F_{vj}$ ) are used to compute the flow field. A 4th-order Runge-Kutta method is applied for the time integration, and the simulations are performed until the maximum residual reaches a small value on the order of  $10^{-15}$ . A full implicit scheme[2] can also be used for fast convergence. The code works in parallel using MPI libraries over hundreds of thousands of cores. Validation of the code for calorically perfect gas and thermal-chemical non-equilibrium flow can be found in our previous studies[2, 3]. Treating the shock wave as a sharp interface allows high accuracy in the flow field, an essential prerequisite for the stability analysis.

The second code is a well-validated fluid dynamic shock capture solver OPENCFD, developed by Li[6], which was mainly used to simulate the nonlinear development of the stationary modes along the wall surface. Inviscid terms are subject to local Lax-Friedrichs splitting and discretised with a seventh-order weighted essentially non-oscillatory scheme. The viscous terms are discretised with an explicit eighth-order centre finite-difference scheme, and time integration is performed using a third-order total variation diminishing-type Runge–Kutta method.

The cross-validation of the two solvers, the detailed grid distributions for the simulations presented in this paper, and the verifications of the grid independence are given in the appendix A.

## 2.3 Boundary conditions

A no-slip boundary condition and the isothermal wall over the surface are employed for shock fitting and capture simulations. At the end of streamwise or surface tangential direction for the computational domain, characteristic non-reflect boundary conditions are imposed.

As one of the primary focus of the present study is to characterize the general behavior of the secondary instabilities of stationary vortices in a relative real hypersonic boundary layer, the disturbances are introduced by using steady wall-normal blowing and suction strip regions. The generator strip is

$$v_n(x, y, z) = \mathscr{A} \sin^3(\pi \frac{x - x_s}{x_e - x_s}) \cos(\beta z), \quad x_s \leqslant x \leqslant x_e, \tag{6}$$

where  $v_n$  is perturb velocity along wall normal directions,  $\mathscr{A}$  is the amplitude of the disturbance.  $x_s$  and  $x_e$  indicate the region of the strip. Several groups used the same function for studying the Görtler instabilities. Due to the shorter flow distance of the model, to ensure that the disturbance can develop to saturation within this distance, we chose a larger initial disturbance for the nonlinear and secondary instability analysis, with the disturbance amplitude reaching 15% of the free stream velocity.

# 2.4 Stability Theory

Over the concave surface, the global streamwise curvature,  $K = -(Re_{\infty}R_2)^{-1}$ , is  $-3.4 \times 10^{-8}$ . The region of interest is over the concave surface, where  $x \in [1,106]\,\mathrm{mm}$ , resulting in  $Re_l = \sqrt{Re_{\infty}x} \in [120,1243]$  and a Görtler number  $G = Re_l\sqrt{\delta_x/R_2} \in [0.246,8.12]$ . Here,  $\delta_x = \sqrt{x/Re_{\infty}}$  stands for a rough estimation of the boundary layer length scale. The linear navier-stokes equations around a stationary state  $\mathbf{Q}_0$  can be represented by the combination of linearised operators and perturbation  $\mathbf{p} = (\hat{\rho}, \hat{u}, \hat{v}, \hat{w}, \hat{T})$  field. This process forms a linear system that can be expressed as

$$\Gamma \frac{\partial \mathbf{p}}{\partial t} + \mathbf{A} \frac{\partial \mathbf{p}}{\partial x} + \mathbf{B} \frac{\partial \mathbf{p}}{\partial y} + \mathbf{C} \frac{\partial \mathbf{p}}{\partial z} + \mathbf{D} \mathbf{p} =$$

$$\mathbf{H}_{xx} \frac{\partial^{2} \mathbf{p}}{\partial x^{2}} + \mathbf{H}_{xy} \frac{\partial^{2} \mathbf{p}}{\partial x \partial y} + \mathbf{H}_{xz} \frac{\partial^{2} \mathbf{p}}{\partial x \partial z} + \mathbf{H}_{yy} \frac{\partial^{2} \mathbf{p}}{\partial y^{2}} + \mathbf{H}_{yz} \frac{\partial^{2} \mathbf{p}}{\partial y \partial z} + \mathbf{H}_{zz} \frac{\partial^{2} \mathbf{p}}{\partial z^{2}},$$

$$(7)$$

where the coefficient matrix  $\Gamma$ , A, B, C, D,  $H_{xx}$ ,  $H_{xy}$ ,  $H_{xz}$ ,  $H_{yy}$ ,  $H_{yz}$ ,  $H_{zz}$  can be found in our previous studies. We further assume that the perturbations take the harmonic forms as

$$p(\xi, \eta, z) = \begin{cases} p'(\eta) \exp[i(\alpha \xi + \beta z)] + c.c., & \text{Local theory,} \\ p'(\eta, z) \exp[i(\alpha \xi)] + c.c. & \text{Bi-Global theory,} \end{cases}$$
(8)

where  $(\xi,\eta)$  are defined in figure 1. With the assumptions, the whole system can be transformed into a large linear complex eigenvalues systems, which can be solved very efficiently using iterative eigenvalue solvers together with the linear solvers such as MUMPS in modern high-performance computing systems.

The evolution of stationary perturbations along the model surface is computed by solving the fully three-dimensional compressible Navier-Stokes equations, which results in steady vortices over the surface.

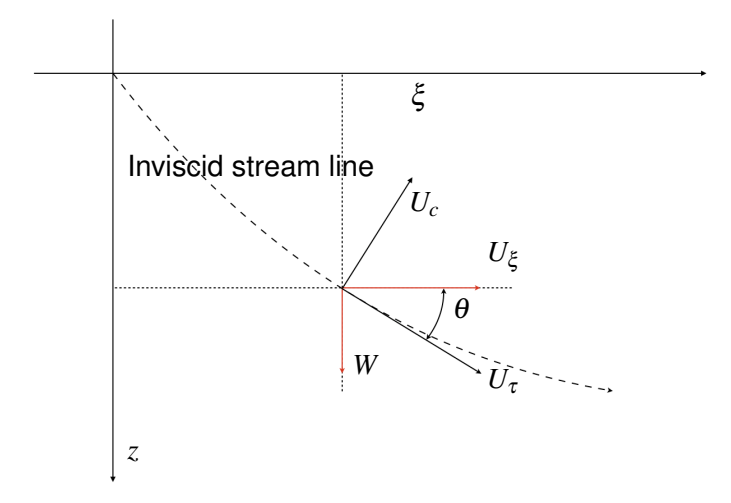


Figure 2 – Sketch of the cross-flow coordinate.  $U_{\xi}$  is the velocity along  $\xi$  direction,  $U_{\tau}$  stands for the velocity along inviscid stream line outside of the boundary layer and  $U_c$  defines the cross-flow.

## 3. Mean flow analysis

The cross flow is defined based on the direction of inviscid stream line outside of the boundary layer and the edge of the boundary layer is defined at the location where the spanwise velocity W reaches 99% of the external velocity  $W_2$ . For simplicity, all the variables on the edge of boundary layer are denoted with the superscript e. As shown in figure 2, the velocity  $U_{\tau}$  and  $U_c$  are defined as

$$U_{\tau} = U_{\xi} \cos \theta + W \sin \theta,$$
  

$$U_{c} = U_{\xi} \sin \theta - W \cos \theta,$$
(9)

where the local streamline angle  $\theta$  is defined as

$$\theta = \arctan\left(W^e/U_{\xi}^e\right). \tag{10}$$

The typical pressure distribution is depicted in figure 3, where the flow commences from the stagnation point and progresses downstream, accompanied by a decrement in pressure. Under the influence of the favourable pressure gradient, the fluid experiences a gradual acceleration. With the augmentation of the swept angle, there is a comprehensive reduction in the pressure level across the entire region. This reflects the phenomenon where an increase in the swept angle results in a greater proportion of the incoming fluid's energy being converted into kinetic energy along the direction of the swept. As the flow further progresses, the flow field extends to the subsequent concave surface, as shown in figure 3 (b). Owing to the high pressure generated in the region of the leading head, the flow continues to develop under a favourable pressure gradient at the front of the concave surface. Conversely, at the rear of the concave surface, the favourable pressure gradient gradually diminishes, and under conditions of a larger swept angle, a slight adverse pressure gradient may even emerge.

# 3.1 Estimations of the instability based on streamline curvatures

Based on previous studies, the origin of both the crossflow and Görtler instability is due to the imbalance between the pressure gradient and centripetal/centrifugal forces. As the centripetal/centrifugal forces result from a locally circular motion, evaluating the forces by fluid movements is natural. Moreover, based on boundary layer theory, the pressure remains nearly unchanged across the boundary layer. Therefore, the inviscid streamline, which reflects both the movements of fluid and the surface pressure distributions, becomes a reliable choice for evaluating these factors. Moreover, if the inviscid streamline keeps straight, neither Görtler nor crossflow instability would occur. Thus, we further assume that the bending of the inviscid streamlines over the surface can be used to evaluate the strength of Görtler or crossflow instability.

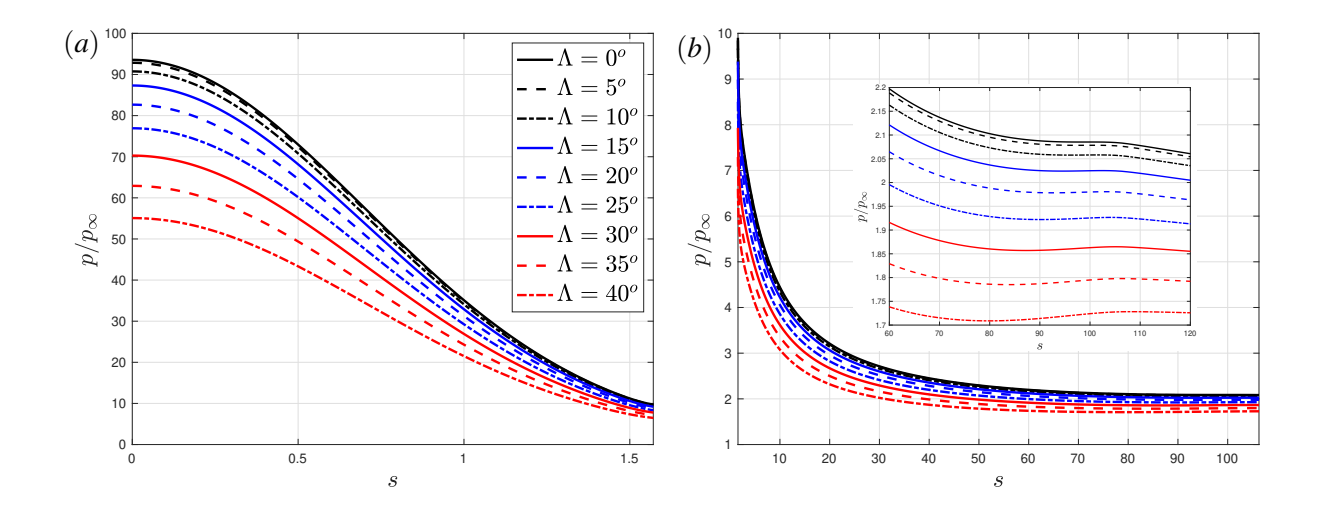


Figure 3 – Steady pressure distribution along the model surface. (a) stands for the cylindrical head with radius  $R_1$  and (b) represents the following flared body with radius  $R_2$ . In figure (b), the region  $(s \in [60, 110])$  is enlarged for clarity.

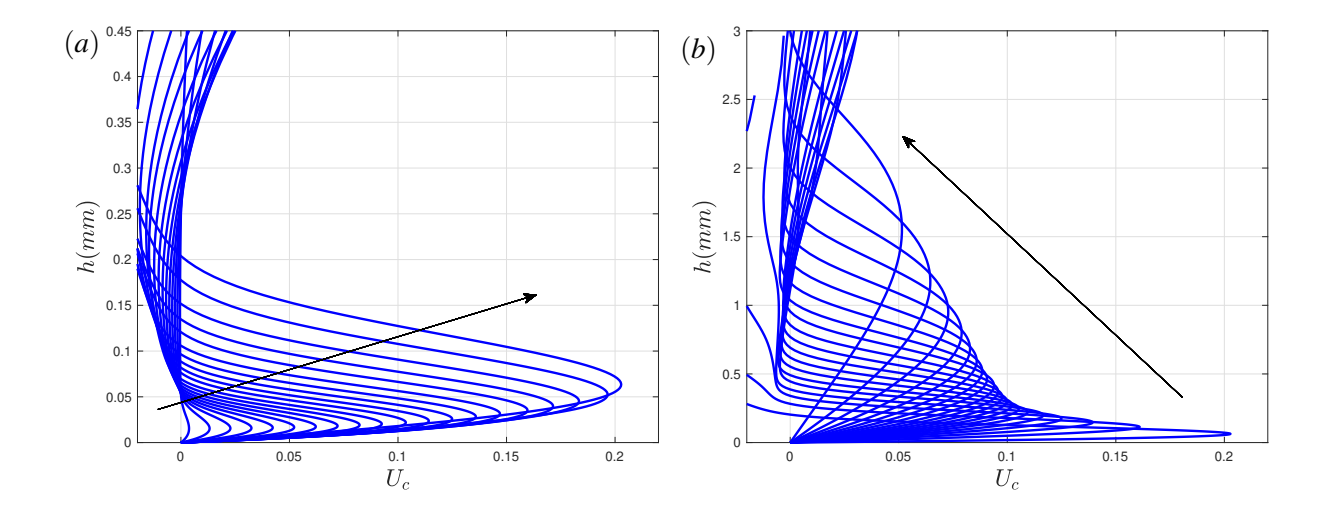


Figure 4 – The profiles of cross-flow velocity  $U_c$  along the surface, for Case 9. (a) stands for the cylindrical head with radius  $R_1$  and (b) represents the following flared body with radius  $R_2$ . The arrows indicate the direction of increasing s.

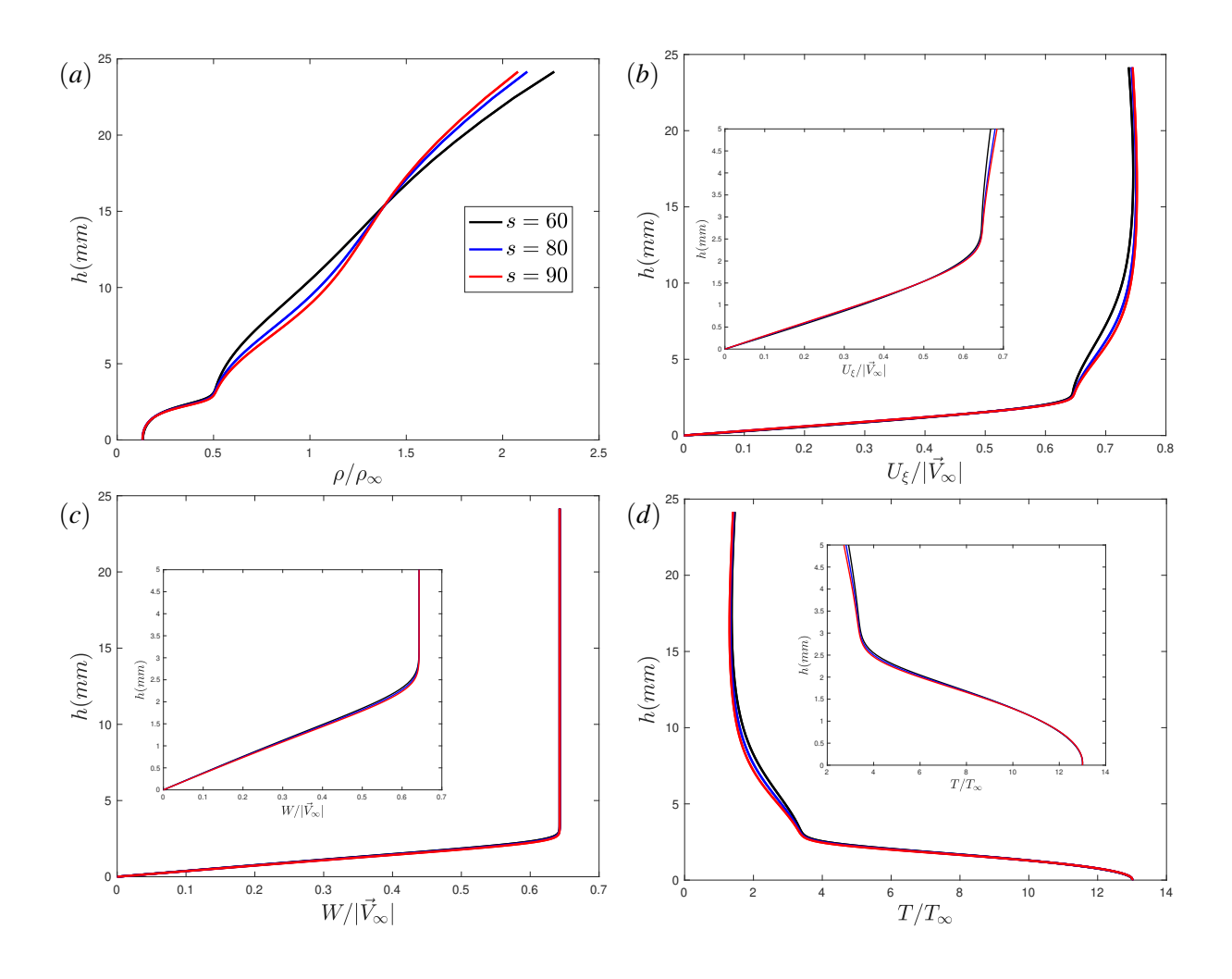


Figure 5 – The profiles of variables along wall normal direction at locations (s=60,80 and 90) from the wall surfaces to the shock surfaces, for Case 9. (a)-(d) stand for the profiles of density  $\rho$ , surface parallel velocity  $U_{\xi}$ , spanwise velocity W and temperature T. The region of boundary is enlarged in (b),(c) and (d).

For the three-dimensional boundary layer in this study, the bending of the streamline is caused by two factors. One is due to the bending of the curved surface, which can be measured by the normal curvature  $\mathcal{K}_n$  concerning the direction of specific streamlines. The other is due to the bending of the streamline inside the surface, which is described by geodesic curvature  $\mathcal{K}_g$ . These two curvatures, together with the general curvature  $\mathcal{K}$  of this streamline, can form the classical geometric relation[7] below:

$$\mathcal{K}^2 = \mathcal{K}_n^2 + \mathcal{K}_o^2. \tag{11}$$

The preceding discussion merely constitutes a qualitative analysis. To delve deeper into a quantitative elucidation of how these curvatures influence the associated disturbances, we present the equations for the local disturbance, considering both geodesic and normal curvatures on the curved surface. For this purpose, we have chosen to employ a local geodesic coordinate system. In this locally orthogonal coordinate system,  $(g_1, g_2, g_3)$ , one axis,  $g_1$ , aligns with the tangent direction of the inviscid streamline, as shown in figure 2. In contrast, another axis,  $g_2$ , aligns with the normal vector of the curved surface along the direction of the inviscid streamline's tangent. In conjunction with the first two, the third axis,  $g_3$ , forms a comprehensive right-handed system. In non-orthogonal curvilinear coordinates, the differentiation between covariant and contravariant components is a well-established concept. Nonetheless, this distinction becomes non-existent within the context of orthogonal curvilinear coordinate systems. The scale factors  $h_{1,2,3}$  of the coordinate system can be expressed as

$$\begin{cases}
h_1^2 = \left(\frac{\partial x}{\partial g_1}\right)^2 + \left(\frac{\partial y}{\partial g_1}\right)^2 + \left(\frac{\partial z}{\partial g_1}\right)^2, \\
h_2^2 = \left(\frac{\partial x}{\partial g_2}\right)^2 + \left(\frac{\partial y}{\partial g_2}\right)^2 + \left(\frac{\partial z}{\partial g_2}\right)^2, \\
h_3^2 = \left(\frac{\partial x}{\partial g_3}\right)^2 + \left(\frac{\partial y}{\partial g_3}\right)^2 + \left(\frac{\partial z}{\partial g_3}\right)^2,
\end{cases} (12)$$

Then, the general curvature components  $\mathcal{K} = \kappa_{ij}$  for arbitary three-dimensional coordinate can be expressed as

$$\mathcal{K} = \begin{bmatrix} \frac{1}{h_1 h_1} \frac{\partial h_1}{\partial g_1}, & \frac{1}{h_1 h_2} \frac{\partial h_1}{\partial g_2}, & \frac{1}{h_1 h_3} \frac{\partial h_1}{\partial g_3} \\ \frac{1}{h_2 h_1} \frac{\partial h_2}{\partial g_1}, & \frac{1}{h_2 h_2} \frac{\partial h_2}{\partial g_2}, & \frac{1}{h_2 h_3} \frac{\partial h_2}{\partial g_3} \\ \frac{1}{h_3 h_1} \frac{\partial h_3}{\partial g_1}, & \frac{1}{h_3 h_2} \frac{\partial h_3}{\partial g_2}, & \frac{1}{h_3 h_3} \frac{\partial h_3}{\partial g_3} \end{bmatrix}$$
(13)

Not all of them appear in the present coordinates. One can find that the axes  $g_2$  and  $\eta$  are both in the surface normal direction. Therefore, the scale coefficient  $h_2$  remains a unit in the abovementioned relationship. The remaining curvature terms can be divided into two sets: the in-plane curvature terms and surface curvature terms, which can be expressed as

in-plane curvature terms: 
$$\kappa_{13} = \frac{1}{h_1 h_3} \frac{\partial h_1}{\partial g_3}, \ \kappa_{31} = \frac{1}{h_1 h_3} \frac{\partial h_3}{\partial g_1},$$
 surface curvature terms: 
$$\kappa_{12} = \frac{1}{h_1 h_2} \frac{\partial h_1}{\partial g_2}, \ \kappa_{32} = \frac{1}{h_3 h_2} \frac{\partial h_3}{\partial g_2},$$
 (14)

with some simple analysis based on classical differential geometry, we can express these curvature terms as a function of local streamline angle  $\theta$  and the distance h away from the surface :

$$\mathcal{K}_{g} = \kappa_{13} = \frac{\partial \theta}{\partial \xi} \cos(\theta), \kappa_{31} = -\frac{\partial \theta}{\partial \xi} \sin(\theta), 
\mathcal{K}_{n} = \kappa_{12} = -\frac{\cos^{2}(\theta)}{R_{2} + h}, \kappa_{32} = -\frac{\sin^{2}(\theta)}{R_{2} + h},$$
(15)

and the scale factors can be expressed as

$$\begin{cases} h_1 = (1 + \mathcal{K}_g g_3)(1 + \mathcal{K}_n g_2), \\ h_2 = 1, \\ h_3 = (1 + \kappa_{31} g_1)(1 + \kappa_{32} g_2), \end{cases}$$
(16)

## 3.1.1 Inviscid analysis

Before further analysis, we look at the inviscid equation in this new coordinate. The inviscid equation can be written as

$$\begin{cases}
\frac{1}{h_{1}} \frac{\partial(\rho u_{g})}{\partial g_{1}} + \frac{\partial(\rho v_{g})}{\partial g_{2}} + \frac{1}{h_{3}} \frac{\partial(\rho w_{g})}{\partial g_{3}} + \kappa_{31} \rho u_{g} + (\mathcal{K}_{n} + \kappa_{32}) \rho v_{g} + \mathcal{K}_{g} \rho w_{g} = 0, \\
\rho \left( \frac{u_{g}}{h_{1}} \frac{\partial u_{g}}{\partial g_{1}} + \frac{v_{g}}{h_{2}} \frac{\partial u_{g}}{\partial g_{2}} + \frac{w_{g}}{h_{3}} \frac{\partial u_{g}}{\partial g_{3}} + \mathcal{K}_{n} u_{g} v_{g} + \mathcal{K}_{g} u_{g} w_{g} - \kappa_{31} w_{g} w_{g} \right) = -\frac{1}{h_{1}} \frac{\partial \rho}{\partial g_{1}}, \\
\rho \left( \frac{u_{g}}{h_{1}} \frac{\partial v_{g}}{\partial g_{1}} + \frac{v_{g}}{h_{2}} \frac{\partial v_{g}}{\partial g_{2}} + \frac{w_{g}}{h_{3}} \frac{\partial v_{g}}{\partial g_{3}} - \kappa_{32} w_{g} w_{g} - \mathcal{K}_{n} u_{g} u_{g} \right) = -\frac{\partial \rho}{\partial g_{2}}, \\
\rho \left( \frac{u_{g}}{h_{1}} \frac{\partial w_{g}}{\partial g_{1}} + \frac{v_{g}}{h_{2}} \frac{\partial w_{g}}{\partial g_{2}} + \frac{w_{g}}{h_{3}} \frac{\partial w_{g}}{\partial g_{3}} + \kappa_{31} u_{g} w_{g} + \kappa_{32} v_{g} w_{g} - \mathcal{K}_{g} u_{g} u_{g} \right) = -\frac{1}{h_{3}} \frac{\partial \rho}{\partial g_{3}}, \\
\frac{u_{g}}{h_{1}} \frac{\partial T}{\partial g_{1}} + \frac{v_{g}}{h_{2}} \frac{\partial T}{\partial g_{2}} + \frac{w_{g}}{h_{3}} \frac{\partial T}{\partial g_{3}} - \frac{(\gamma - 1)}{\rho} M a^{2} \left( \frac{u_{g}}{h_{1}} \frac{\partial \rho}{\partial g_{1}} + \frac{v_{g}}{h_{2}} \frac{\partial \rho}{\partial g_{2}} + \frac{w_{g}}{h_{3}} \frac{\partial \rho}{\partial g_{3}} \right) = 0.
\end{cases}$$

in which the terms related to curvature are highlighted in blue and blue. If ignoring the bending effects of the third axis  $g_3$  ( $\kappa_{31}=\kappa_{32}=0$ ), and remembering that in this coordinate, in the inviscid limit, the major velocity terms over the surface are  $u_g$  and  $w_g$ , the contributions to the variations of meanflow can be seen as the consequences of the red terms, in which the geodesic curvature and normal curvature are directly shown.

## 3.1.2 Production analysis

Then, we drive the production term  $P_g^{dis}$  of the perturbation energy  $E_g^{dis}$ . Following the equations in the analysis of compressible turbulence, the perturbation energy here is defined as

$$E_g^{dis} = \frac{1}{2}\hat{\rho} \left( \hat{u}^2 + \hat{v}^2 + \hat{w}^2 \right) \tag{18}$$

Therefore, the general production terms for disturbances can be expressed as

$$P_g^{dis} = -\overline{\rho}\,\sigma_{ij}\tilde{S}_{ji}.\tag{19}$$

Given the stationary mean flow without perturbations, it can be simplified for the present cases as

$$P_g^{dis} = -\rho \,\sigma_{ij} S_{ji},\tag{20}$$

In accordance with the widely accepted local parallelism assumption prevalent in local theoretical frameworks, upon excluding terms devoid of curvature contributions, it becomes feasible to assess the influence of curvature on the system quantitatively. The curvature contributions  $P_g^{cur}$  can be expressed as

$$P_{g}^{cur} = -\rho \mu \begin{bmatrix} \left( \mathcal{K}_{g}^{2} + \mathcal{K}_{n}^{2} + \frac{4}{3} \kappa_{31}^{2} \right) u_{g}^{2} + \left( -2 \mathcal{K}_{n} \frac{\partial u_{g}}{\partial g_{2}} \right) u_{g} + \\ \left( \kappa_{31}^{2} + \kappa_{32}^{2} + \frac{4}{3} \mathcal{K}_{g}^{2} \right) w_{g}^{2} + \left( -2 \kappa_{32} \frac{\partial w_{g}}{\partial g_{2}} \right) w_{g} + \\ \frac{2}{3} \mathcal{K}_{g} \kappa_{31} u_{g} w_{g}, \end{cases}$$
(21)

in which  $u_g$ ,  $w_g$  are the velocity along  $g_1$  and  $g_3$ . In the ensuing analysis, this expression (21) is divided into two scenarios. The first scenario exclusively considers the condition with surface curvature but without in-plane curvature, wherein the corresponding steady flow instability is governed by the

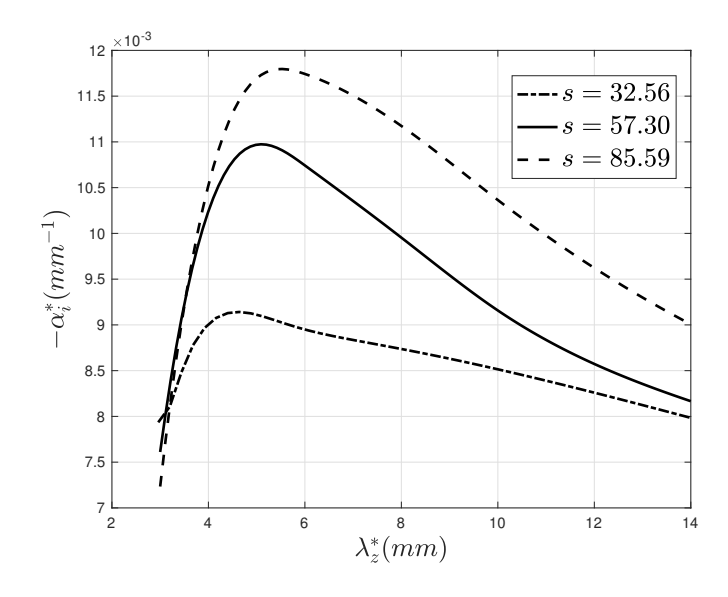


Figure 6 – Variations of growth rate to span-wise wave length at different location for the unswept case.

Görtler mechanism. In the second scenario, we solely consider the condition with in-plane curvature but without surface curvature, at this juncture, the steady flow instability is controlled by the crossflow mechanism. Therefore, we have the following relationship

Part 1 
$$\begin{cases} \mathcal{K}_{g} = \kappa_{31} = 0, \\ P_{g}^{cur,1} = -\rho\mu \left[ \mathcal{K}_{n}^{2}u_{g}^{2} - 2\mathcal{K}_{n}\frac{\partial u_{g}}{\partial g_{2}}u_{g} + \kappa_{32}^{2}w_{g}^{2} - 2\kappa_{32}\frac{\partial w_{g}}{\partial g_{2}}w_{g} \right] \\ \text{Part 2} \begin{cases} \mathcal{K}_{n} = \kappa_{32} = 0, \\ P_{g}^{cur,2} = -\rho\mu \left[ \left( \mathcal{K}_{g}^{2} + \frac{4}{3}\kappa_{31}^{2} \right)u_{g}^{2} + \left( \frac{4}{3}\mathcal{K}_{g}^{2} + \kappa_{31}^{2} \right)w_{g}^{2} + \frac{2}{3}\mathcal{K}_{g}\kappa_{31}u_{g}w_{g} \right] \end{cases}$$
(22)

This expression clearly delineates that the normal curvature of the surface along the direction of inviscid streamline is positively correlated with the disturbance intensity induced by the corresponding Görtler mechanism. Furthermore, the geodesic curvature of the inviscid streamline within the curved surface is also positively correlated with the disturbance induced by the corresponding crossflow mechanism.

## 4. Stability analyses

#### 4.1 primary instability

The primary instability analysis are performed to identify the basic features of the perturbations.

At first, we look at the local behaviour of the three-dimensional boundary layer over the whole surface that we care about. Figure 6 shows the variation of local growth rate to spanwise wave length  $\lambda_z$  at three typical stream-wise location for unswept case. One can found that the growth rates reach their peaks at around the region [4mm, 6mm], and then decrease at larger wave length. As in this case, no swept angle is presented, the only mechanism that leads to steady disturbance is due to the Görtler mechanism. Tracing the behaviour of the most unstable one, we choose the  $\lambda_z = 5.53mm$  as the typical parameter for the primary instability analysis.

Then we put all cases together in figure 7 and one can identify two trends as soon as possible, the black group and the blue one. The black line for case 4 can be seen as a general boundary for the 'transition' of the two trend. The case 1 to case 3, the growth rate increase with the increasing of swept angle and can be seen as the effects of Görtler mechanism. Also, as the swept angle incease, the growth rate become much smaller. On the other hand, the blue lines with respect to case 5 to case 8 are due to the crossflow mechanism. From this figure, we can roughly identify that as the

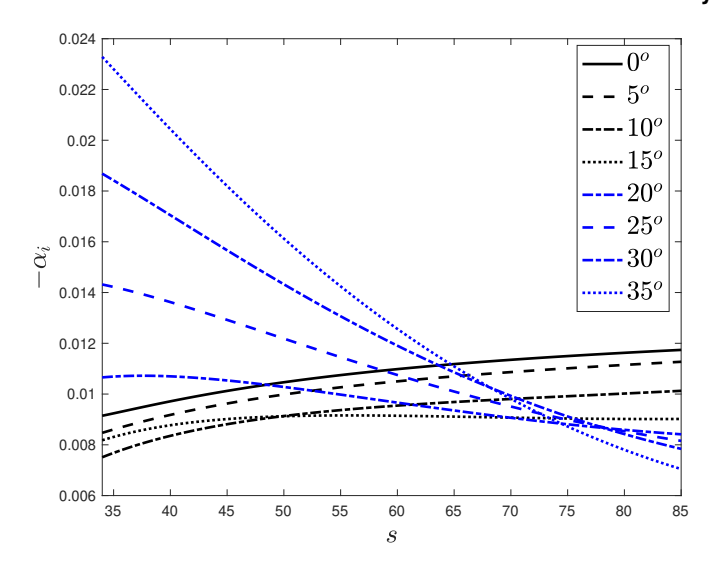


Figure 7 – Variations of growth rate to different stream-wise location for different swept angles.

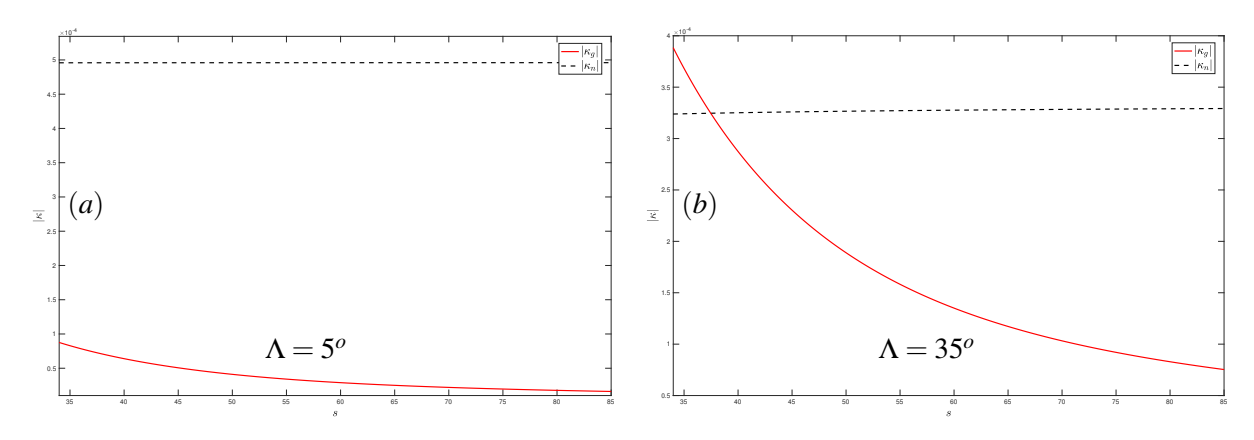


Figure 8 – Comparison of the normal curvature and geodesic for cases with swept angle  $\Lambda = 5^o$  and  $\Lambda = 35^o$ 

swept angle increase, the Görtler mechanism will be depressed by the crossflow mechanism and the at larger swept angle, the crossflow mechanism will become the dominate.

Therefore, we can partially understand our results from geometrical point of view, as shown in figure 8. As the swept angle increase, the normal curvature will decrease, which is directly connected to the decrease of growth rate of the unstable mode due to the Görtler effect. Meanwhile, the geodesic curvature increases and when the geodesic curvature become the dominate one (as shown in figure 8(b)), the crossflow effect will become the dominate.

## 4.2 Nonlinear saturations and secondary instabilities

## 4.2.1 Nonlinear developments

The nonlineaer saturations for both cases are simulated by solving the Navier-stokes equations directly, with the steady blowing and suction perturbations of the spanwise wavelength 6mm. The relative evolutions are shown in figure 9 and figure 10, with the help of contours of temperature  $T/T_{\infty}$  at the side slices as well as the velocity component  $u_1/|\vec{V}_{\infty}|$ . As the initial perturbations are large enough (about 15% of the freestream velocity), the perturbations are grow rapidly beyound the linear region and reach their nonlinear saturations in a short distance, as shown in the heat fluxes in appendix A. From figure 9 and figure 10, a clear trends of the transformations between the Görtler vortices and Crossflow vortices can be identified.

After obtaining a general understanding of steady perturbations, we introduce the concept of perturbation energy  $E(\mathbf{p}_0, \mathbf{p})$  for a more precise description of the nonlinear development of the perturba-

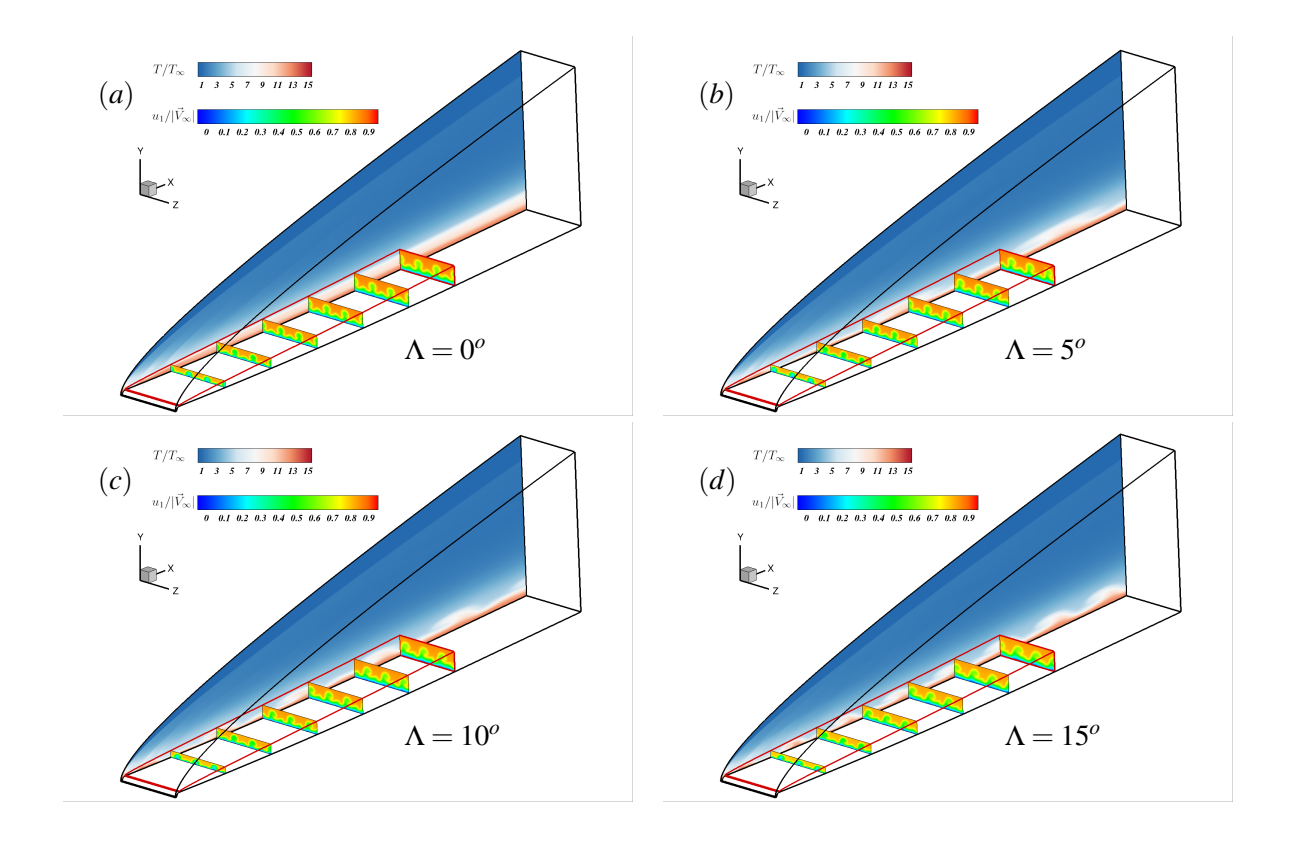


Figure 9 – Nonlinear development of steady vortices. (a)  $\Lambda = 0^{o}$ , (b)  $\Lambda = 5^{o}$ , (c)  $\Lambda = 10^{o}$ , (d)  $\Lambda = 15^{o}$ .

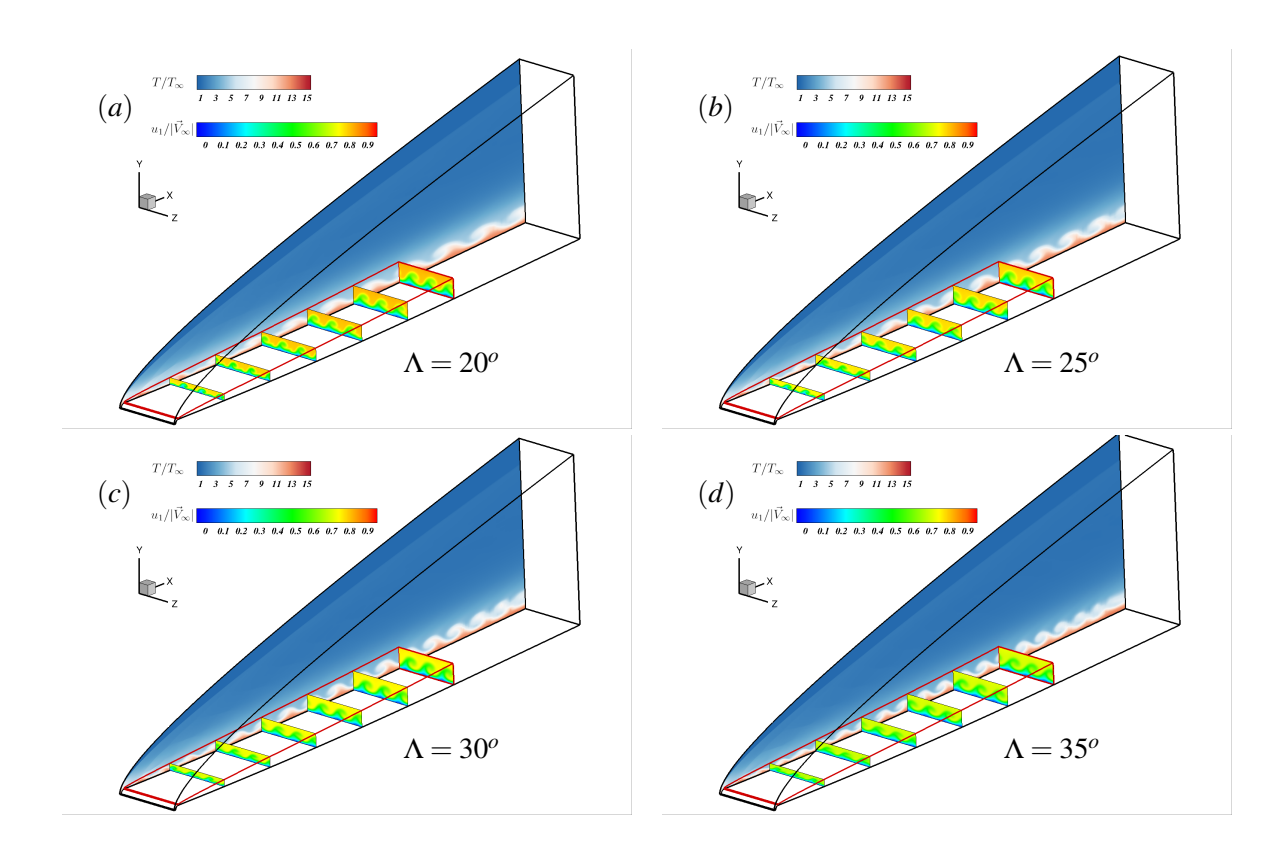


Figure 10 – Nonlinear development of steady vortices. (a)  $\Lambda=20^o$ , (b)  $\Lambda=25^o$ , (c)  $\Lambda=30^o$ , (d)  $\Lambda=40^o$ .

tions. It is important to note that these perturbations p are defined relative to the laminar basic flow  $p_0$ . The corresponding perturbation energy is defined based on a weighted integral over a spatial plane perpendicular to the wall, as a norm:

$$E(\mathbf{p}_0, \mathbf{p}) = \frac{1}{3} \iint_{\eta, z} (\mathbf{p}^T \mathbf{M} \mathbf{p}) dz d\eta,$$
 (23)

where

$$\boldsymbol{p}_{0} = \left(\boldsymbol{\rho}, \boldsymbol{u}, \boldsymbol{v}, \boldsymbol{w}, T\right)^{T}, \boldsymbol{p}_{0} = \left(\hat{\boldsymbol{\rho}}, \hat{\boldsymbol{u}}, \hat{\boldsymbol{v}}, \hat{\boldsymbol{w}}, \hat{T}\right)^{T}, \boldsymbol{M} = \begin{bmatrix} \frac{T}{\gamma \rho M_{\infty}^{2}} & & & & \\ & \boldsymbol{\rho} & & & \\ & & \boldsymbol{\rho} & & \\ & & & \frac{\rho}{\gamma (\gamma - 1)TM_{\infty}^{2}} \end{bmatrix}$$

The coefficient 1/3 is used here as there are three obvious streaks in the present paper. Based on the norm definition, both kinetic energy and the thermodynamic energy of the perturbations are taken into account. The distributions of perturbation energy for different cases along the surface are shown in figure 11. The evolution processes of the disturbance energy are normalized by the disturbance energy  $E_0$  at x=10 (the artificial unsteady disturbance is added in the interval  $x \in [5,10]$ ) to facilitate a more rational comparison of disturbance evolution under different conditions. Except for the two cases with the largest sweep angles, disturbances exhibit significant transient growth characteristics in the downstream region after being excited under other conditions, manifested as an exponential increase in disturbance energy. In the cases corresponding to sweep angles of 35 and 40 degrees, the disturbances show a distinct attenuation characteristic in the downstream region. After the disturbance propagates downstream along the flow direction for some time, the attenuation rate gradually decreases, followed by a noticeable increase in disturbance energy. Due to the relatively large disturbances added, the corresponding streaks quickly reach a saturation state. According to the nonlinear evolutions of the corresponding streaks, in the absence of other influencing mechanisms, the saturated streaks will continue to decay unless secondary instabilities occur. However, in the working condition of our study, the surface is concave, thus presenting a negative curvature in the  $\xi$  direction. Under the effect of this negative curvature, the decay process of the disturbance streak energy is suppressed, leading to a subsequent increase in the corresponding disturbance energy. It should also be noted that there exists a very weak pressure gradient on this concave surface. The evolution process of the corresponding streaks should be the result of the combined effects of the pressure gradient and curvature.

#### 5. Conclusions

This study has delved into the intricacies of hypersonic boundary layer instabilities, a pivotal factor in the design of hypersonic vehicles, by conducting detailed numerical simulations and theoretical analyses. Our work has highlighted the complex interplay between crossflow and Görtler instabilities in three-dimensional flows over concave surfaces, with a particular emphasis on the role of streamline curvature. The research indicates that crossflow instability generally prevails in shaping the transition from laminar to turbulent flow, especially when the flow encounters significant swept angles.

The critical influence of the streamline curvature's normal and geodesic components has been underscored, revealing that their ratio is a determining factor for the onset of instabilities. Interestingly, the Görtler instability, while typically secondary to crossflow, can become a primary concern under specific conditions where the normal curvature overtakes the geodesic curvature in influence.

Furthermore, the dynamics between the instabilities are not isolated; our findings suggest that as the flow evolves, secondary instabilities may influence the transition process, particularly during the nonlinear stages. The implications of this study are far-reaching, offering essential insights for the hypersonic community. These insights lay the groundwork for future experimental setups and provide guidance for the optimization of vehicle surface designs to mitigate transition risks.

Looking ahead, there is a rich landscape of opportunities for research to broaden the understanding of instability mechanisms under varying geometries and operational conditions. Developing strategies to effectively manage the laminar-turbulent transition remains a key objective, with the potential to significantly improve the aerodynamic performance and efficiency of hypersonic vehicles.

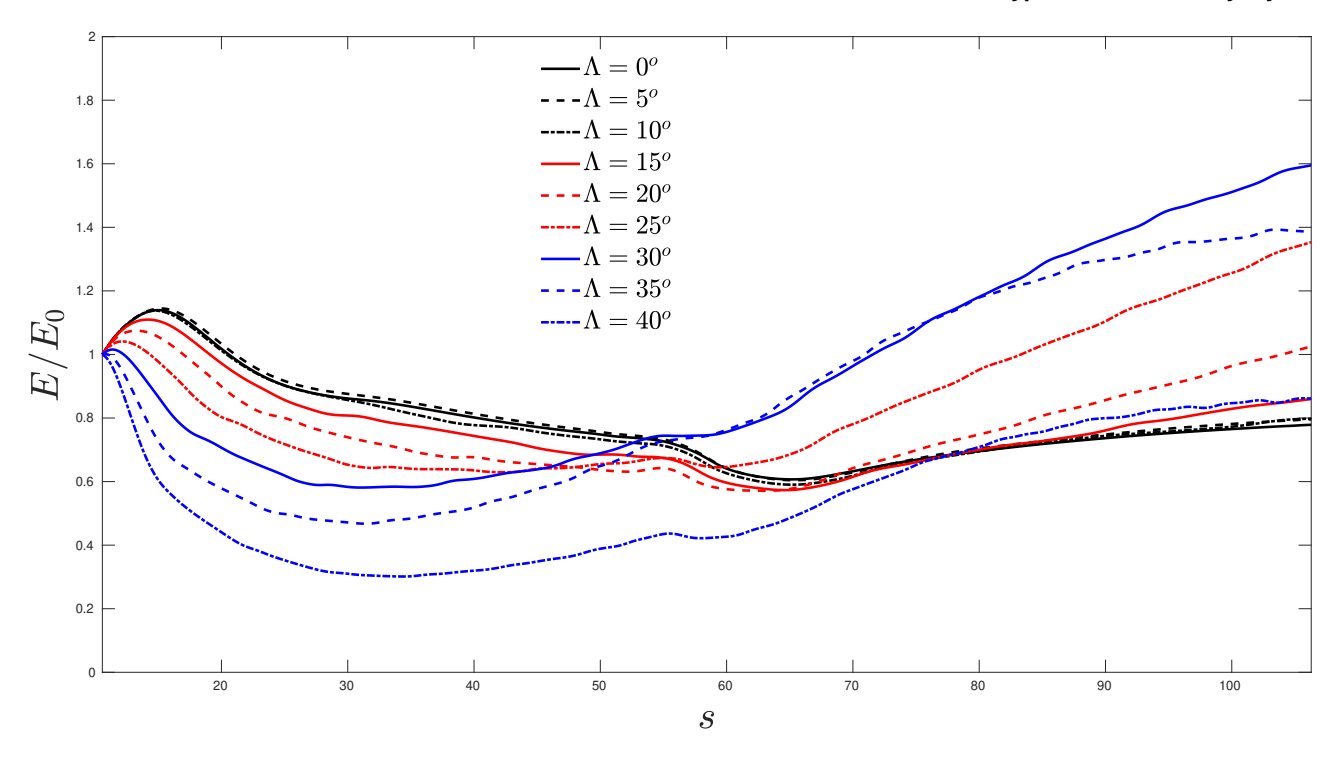


Figure 11 – The distributions of perturbation energy for different cases along the surface.

# Acknowledgement

This work received partial support from the NSFC Grants 12202242, 12172195 and 12388101. The authors are also grateful for the support from the National Key Research and Development Plan of China through project no. 2019YFA0405201 and the National Key Project GJXM92579.

#### A Validations and verifications

## 1.1 Grid distributions for shock-fitting solver

The basic grid number used for shock-fitting simulations is  $N_{\xi} \times N_{\eta} \times N_{z} = 1201 \times 141 \times 8$ . The distribution of the grid points in the wall-normal direction is controlled through a function that provides clustering towards the wall, with two parameters  $h_{im}$  and  $\sigma_{s}$ . The distribution function, which maps  $\eta$  to h, can be expressed as

$$h = H_{shk} \frac{a_y(1+Y)}{(b_y - Y)}, b_y = 1 + 2a_y, \quad a_y = \frac{h_{im}}{1 - 2h_{im}},$$

$$Y = 2 \frac{\left[1 - \tanh(\sigma_s)\right] \frac{1+\eta}{2}}{1 - \tanh\left(\sigma_s \frac{1+\eta}{2}\right)} - 1,$$
(24)

where  $H_{shk}$  is the local shock height and is solved as a dependent variable with the flow field in shock-fitting methods,  $\eta$  is a uniform grid distribution along the region [-1.0, 1.0], h is the actual wall-normal grid distributions. The values of  $h_{im}$  and  $\sigma_s$  are chosen to be 0.2 and 0.95 for the fitting simulations presented in this paper.

Along the wall surface, the surface grid s(x,y) is clustered at the round head with the function

$$\frac{s}{S} = \frac{a_{\xi}(1-\xi)}{b_{\xi}-\xi}, b_{\xi} = 1 + 2a_{\xi}, a_{\xi} = \frac{s_{im}}{1-2s_{im}},$$
(25)

where  $s_{im}$  is chosen to be 0.05 for the simulations based on shock-fitting methods, s is the local surface curve length along the model surface, and s is the total model surface curve length. Note that the surface grid does not change during the calculation. In our computations, we adopt periodic boundary conditions in the spanwise direction, hence the corresponding computational grid is uniformly distributed.

		$N_{\eta}$ ,		Solver
				Shock-capture
Distribution 2	2201	321	150	Shock-capture
Distribution 3	2201	421	150	Shock-capture

Table 2 – Three grid numbers for grid convergence study.

#### 1.2 Grid distributions for capture solver

The basic grid numbers used for shock-capture simulations is  $N_{\xi} \times N_{\eta} \times N_z = 2201 \times 421 \times 150$ . Unlike the fitting solver, for the capture solver, the wall-normal grid needs clustering towards the wall and in the shock region. Therefore, the wall-normal grid is divided into three parts. The first part is at the region  $[0,0.48H_{shk}]$ . The second part is a transition region which connects the near-wall region and the shock region and is located at the region  $[0.48H_{shk},0.72H_{shk}]$ . The final region stands for the part used to capture the shock and is located at the region  $[0.72H_{shk},1.2H_{shk}]$ . As the local shock height  $H_{shk}$  is solved by the fitting solver in advance, the grid lines are adapted well to both the body and the shock shape. The first region has 301 grid points, with the distributions  $h_1$  as

$$h_1 = 0.48H_{shk}\frac{1+\eta_1}{2-\eta_1},\tag{26}$$

where  $\eta_1$  is the uniform distributions in region [-1,1]. The third region has 81 grid points with a uniform distribution. The second region has 41 grid points and is used to link grids with different grid spacings using a Hermite function obtained by imposing C3 continuity of the resulting stretching function.

We have partitioned the surface grid into five distinct flow regions. The first and second regions are located on the cylinder at the head of the model, the third region corresponds to the complete concave surface, while the fourth and fifth regions pertain to the flat plate at the model's tail. From the symmetry plane to the first two-thirds of the cylinder surface, the first region is uniformly populated with 161 grid points. The third region is uniformly populated with 1921 grid points, while the fifth region is arranged with 51 grid points, with the grid spacing gradually increasing to absorb and reduce non-physical disturbances. The second and fourth regions are respectively arranged with 21 and 51 grid points, in which the C3 continuous smooth functions connect the grids of different intervals to ensure a smooth transition in grid spacing. The spanwise distributions remain the same as in the fitting solver.

#### 1.3 Grid convergence

Several different grid distributions were tested to ensure the results, especially for the nonlinear saturated Görtler or crossflow vortexes. The unswept configuration was chosen as a test case, and three different grid distributions were used for the grid convergence study. The grid numbers are shown in table 2. The spanwise-average heat fluxes calculated over the three different grid distributions are shown in figure 12, as well as the basic state streamwise velocity contours. Excellent agreement between the solutions was found even in the relatively stringent comparisons involving velocity contours across the cross-sectional area of the Görtler vortices.

#### 1.4 Cross validation and verifications of the solvers

We also chose the unforced unswept case as a test case. The calculations were performed over two typical basic grids discussed above with shock-fitting and shock-capture solver. As only the laminar case is considered, the results is obtained through spanwise average. The profiles of several different stations along the *x* coordinate are shown in figure 13, based on the solution at different x-positions. Figure 13 shows a good agreement between the given grids for different methods is reached.

#### **B** Contact Author Email Address

Dr. Youcheng Xi: xiyc@mail.tsinghua.edu.cn, Prof. Song Fu: fs-dem@tsinghua.edu.cn

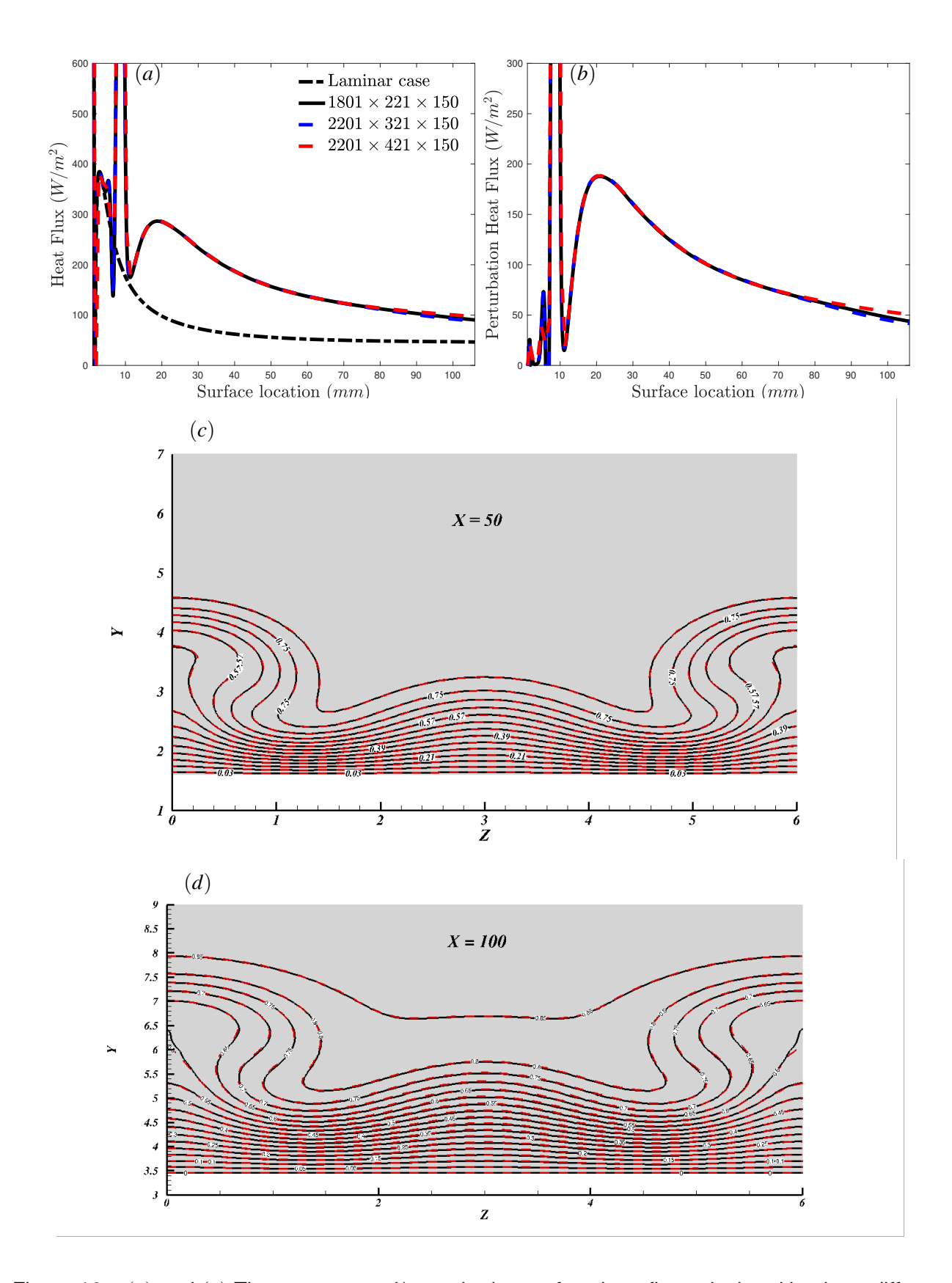


Figure 12 - (a) and (b) The average total/perturbation surface heat flux calculated by three different grid distributions. (c) and (d) stands for the basic state meridional velocity contours at X = 50 and X = 100. The red dashed line shows the solution based on grid distribution 3, and the solid line is the grid distribution 2.

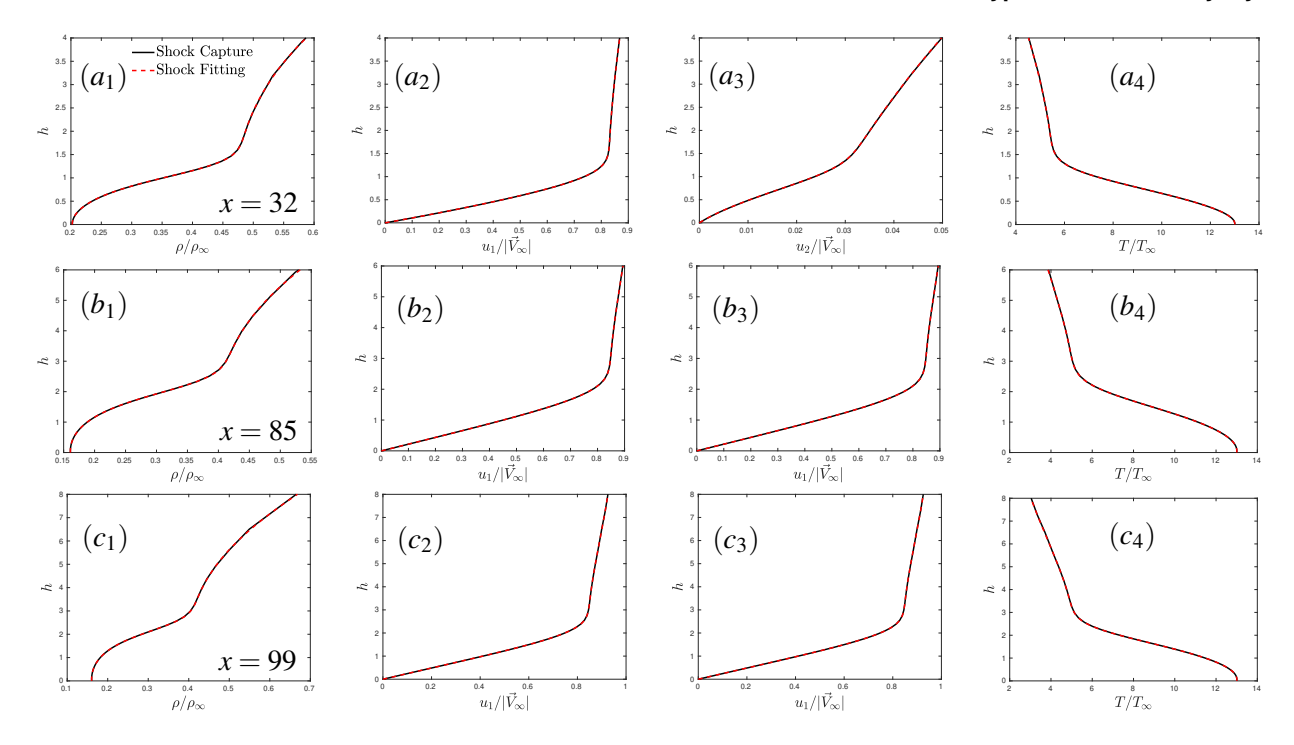


Figure 13 – Comparison of the physical quantity profiles calculated by the Shock-Fitting and Shock-Capture methods over basic grids at different *x* positions.

# **C** Copyright Statement

The authors confirm that they, and/or their company or organization, hold copyright on all of the original material included in this paper. The authors also confirm that they have obtained permission, from the copyright holder of any third party material included in this paper, to publish it as part of their paper. The authors confirm that they give permission, or have obtained permission from the copyright holder of this paper, for the publication and distribution of this paper as part of the ICAS proceedings or as individual off-prints from the proceedings.

#### References

- [1] E. Reshotko and I. E. Beckwith. Compressible laminar boundary layer over a yawed infinite cylinder with heat transfer and arbitrary prandtl number. Report 1379, National Advisory Committee for Aeronautics., 1958.
- [2] Xianliang Chen and Song Fu. Convergence acceleration for high-order shock-fitting methods in hypersonic flow applications with efficient implicit time-stepping schemes. *Computers & Fluids*, 210:104668, 2020.
- [3] Youcheng Xi, Jie Ren, and Song Fu. Hypersonic attachment-line instabilities with large sweep mach numbers. *Journal of Fluid Mechanics*, 915:A44, 2021.
- [4] Youcheng Xi, Jie Ren, Liang Wang, and Song Fu. Receptivity and stability of hypersonic leading-edge sweep flows around a blunt body. *Journal of Fluid Mechanics*, 916:R2, 2021.
- [5] Xiaolin Zhong. High-order finite-difference schemes for numerical simulation of hypersonic boundary-layer transition. *Journal of Computational Physics*, 144(2):662 709, 1998.
- [6] Xinliang Li, Dexun Fu, and Yanwen Ma. Direct numerical simulation of hypersonic boundary layer transition over a blunt cone. *AIAA Journal*, 46(11):2899–2913, 2008.
- [7] Manfredo P. do Carmo. Differential Geometry of Curves and Surfaces. Dover Publications, 2016.